The Cryosphere Discuss., 5, 3221–3258, 2011
www.the-cryosphere-discuss.net/5/3221/2011/
doi:10.5194/tcd-5-3221-2011

The Cryosphere Discussions

Sensitivity of a distributed temperature-radiation index melt model based on a four melt season AWS record from Hurd Peninsula glaciers, Livingston Island, Antarctica

U. Y. Jonsell[1,2], **F. J. Navarro**[1], **M. Bañón**[3], **J. J. Lapazaran**[1], **and J. Otero**[1]

[1]Departamento de Matemática Aplicada, E.T.S.I. Telecomunicación, Universidad Politécnica de Madrid, Av. Complutense, 30, 28040 Madrid, Spain
[2]Swedish Polar Research Secretariat, P.O. Box 50003, 104 05 Stockholm, Sweden
[3]Observatorio Meteorológico de Alicante, Agencia Estatal de Meteorología (AEMET), C/ Regidor Ocaña, 26, 03011 Alicante, Spain

Received: 27 October 2011 – Accepted: 6 November 2011 – Published: 28 November 2011

Correspondence to: U. Y. Jonsell (ulf.jonsell@polar.se)

Published by Copernicus Publications on behalf of the European Geosciences Union.

Abstract

We use an automatic weather station and mass balance dataset spanning four melt seasons collected on Hurd Peninsula Glaciers, South Shetland Islands, to investigate the point surface energy balance, to determine the absolute and relative contribution of the various energy fluxes acting on the glacier surface and to estimate the sensitivity of melt to ambient temperature changes. Long-wave incoming radiation is the main energy source for melt, while short-wave radiation is the most important flux controlling the variation of both seasonal and daily mean surface energy balance. Short-wave and long-wave radiation fluxes do in general balance each other, resulting in a high correspondence between daily mean net radiation flux and available melt energy flux. We calibrate a distributed melt model driven by air temperature and an expression for the incoming short-wave radiation. The model is calibrated with the data from one of the melt seasons and validated with the data of the three remaining seasons. The model results deviate at most 0.14 m w.e. from the corresponding observations using the glaciological method. The model is very sensitive to changes in ambient temperature: a 0.5 °C increase results in 56 % higher melt rates.

1 Introduction

1.1 Background

Retreating and thinning glaciers have come at sharp focus in relation with increased atmospheric temperatures attributed to anthropogenic greenhouse emissions. Air temperature changes and their associated changes in meteorological conditions will, in different ways and to different extent, affect the various fluxes providing energy for heating and melting a glacier surface as part of an intricate system involving several feedback mechanisms (Ohmura, 2001). Surface energy balance (SEB) calculations using automatic weather station (AWS) data from glaciers aim to separate and

TCD
5, 3221–3258, 2011

quantify the contributing fluxes and form a basis for understanding the coupling between meteorological conditions and glacier melt. As a prognostic tool for the response in energy fluxes, and eventually melt rates, to perturbations in meteorological conditions, SEB models have the advantage of being physically based but the disadvantage of involving a complicated extrapolation procedure to distribute the fluxes over the glacier surface (Hock, 2005). To overcome this complexity, the simpler temperature-index models, based on the coupling between energy fluxes and temperature, are widely used. They perform best in environments where long-wave radiation and sensible heat are the dominating energy sources, as those fluxes are strongly coupled to temperature (Ohmura, 2001), while in environments dominated by solar radiation the model performance is reduced (Sicart et al., 2008). In many glaciated areas of the world, long-wave radiation is the major energy source for melt, but short-wave radiation plays a dominant role for the diurnal, daily and inter-seasonal variation of energy available for heat and melt (Greuell and Genthon, 2004). Therefore models including representations of a combination of temperature and short-wave radiation are commonly used (e.g. Hock, 1999; Pellicciotti, et al., 2005; Schuler et al., 2005; Möller et al., 2011).

An increasing number of studies based on AWS data combined with glaciological mass balance data are continuously improving the understanding of glacier SEB and its geographical differences (e.g. Andreasssen et al., 2008; Giesen et al., 2008; Hulth et al., 2010). In this paper we present an AWS record extending over four melt seasons and its associated SEB from a region scarcely represented in the literature, namely the Hurd Peninsula on Livingston Island, South Shetland Islands, an archipelago parallel to the northwestern extreme of the Antarctic Peninsula (Fig. 1). The Antarctic Peninsula region has experienced a remarkable warming during the last decades (Vaughan et al., 2003; Turner et al., 2009). The 41-year long temperature record from Bellinghausen research station on King George Island, located about 90 km to the NE of Hurd Peninsula, shows a 0.25 °C per decade warming (http://www.nerc-bas.ac.uk/icd/gjma/temps.html). The impact of the warming in the

TCD
5, 3221–3258, 2011

region on glacier dynamics (Rott et al., 1996; Rignot et al., 2004; Scambos et al., 2004; Pritchard and Vaughan, 2007), glacier extent (Rau et al., 2004; Cook et al., 2005), mass balance and melt rates (Braun and Hock, 2004; van den Broeke, 2005; Turner et al., 2005, 2009; Vaughan, 2006) are key scientific questions for understanding the contribution of grounded ice losses from this region to future sea level rise. The Hurd Peninsula glaciers mass balance record (Navarro et al., 2011) is the only currently ongoing mass balance programme from the Antarctic Peninsula with both summer and winter balances listed at the World Glacier Monitoring Service, thus providing a particularly suitable field data source for studying the coupling between meteorological conditions and mass balance.

We use the AWS record to briefly outline the meteorological conditions at the site and to quantify the absolute fluxes and their relative contribution to melt. We also apply a distributed temperature-radiation index melt model, which is calibrated with in-situ mass balance data obtained using the glaciological method (Navarro et al., 2011). We compare the melt rates obtained from SEB and temperature-index model at the point scale, and use the four years of AWS data to compare the distributed modelled and measured melts. We use the calibrated model to analyze its sensitivity to changes in meteorological conditions. Furthermore, we present a novel approach to handle sub-daily albedo data that reduces the diurnal variations arisen due to measurement deficiencies but keeps the diurnal variations due to changes in cloud cover.

1.2 Physical setting

The Hurd Peninsula ice cap (62°39–42′ S, 60°19–25′ W; Fig. 1) covers an area of about 13.5 km^2 and spans an altitude range from sea level to about 330 m a.s.l. It is partly surrounded by mountains that reach elevations between 250 and 400 m. Hurd Peninsula ice cap can be subdivided into two main glacier systems, Johnsons glacier, a tidewater glacier, flowing north-westwards, that terminates on an ice cliff about 50 m in height a.s.l. extending approximately 500 m along the coast, and Hurd glacier terminating on land and mainly flowing south-westwards, with ice thickness tapering to

TCD
5, 3221–3258, 2011

zero in the snouts of Sally Rocks, Argentina and Las Palmas. Two other basins are also part of the ice cap, both flowing eastwards towards False Bay. However, these are not included in this study because they are heavily crevassed icefalls preventing field measurements. The local ice divide separating Johnsons and Hurd lies between 250 and 330 m a.s.l. Hurd glacier has an average surface slope of about 3°, though the small westward flowing glacier tongues Argentina and Las Palmas are much steeper (approx. 13°). Typical slopes for Johnsons glacier range between 10° in its northern areas and 6° in the southern ones. The average ice thickness of the ice cap, determined from ground-penetrating radar data in 2000/2001, was 93.6 ± 2.5 m, with maximum values about 200 m in the accumulation area of Hurd glacier (Navarro et al., 2009). The ice surface velocities of Johnsons glacier increase downstream from the ice divide, reaching annual-averaged values up to 65 m a^{-1} at the fastest part of the calving front (Otero et al., 2010), while the largest ice velocities for Hurd glacier are typically about 5 m a^{-1} (Otero, 2008). The Hurd Peninsula ice cap is a polythermal ice mass, showing an upper layer of cold ice, several tens of metres thick, in the ablation area (Molina et al., 2007; Navarro et al., 2009). The cold layer is rather uniform in Hurd glacier, while in Johnsons glacier the layer is more patchy.

The Spanish Antarctic Station Juan Carlos I (JCI) is located very close to Hurd Peninsula ice cap (Fig. 1). Meteorological measurements are maintained in JCI all year round by an AWS, and are complemented by manual meteorological observations during the summer. In December 2006, an AWS was installed on the upper ablation area of Johnsons Glacier (Fig. 1). The latter provides the main meteorological data source used in this paper and will be further described in the next section.

The Hurd Peninsula ice cap is subjected to the maritime climate of the western Antarctic Peninsula region, with some particularities due to local conditions. The orography of Livingston Island alters the regional prevailing northwesterly dominating wind direction. At JCI and Johnsons Glacier the predominant wind direction is from NNE, followed by SSW (JCI), ENE (Johnsons Glacier). Average wind speeds are about 4 m s^{-1}, but gusts wind speeds above 30 m s^{-1} are frequent. The highest wind speeds come

TCD
5, 3221–3258, 2011

from East and North-East directions and are associated with deep westward facing low pressure systems passing north of Livingston Island.

The annual average temperature at JCI during the period 2000–2010 was −1.1 °C, with average summer (DJF) and winter (JJA) temperatures of 2.8 °C and −4.4 °C, respectively, with maximum/minimum registered temperatures of 15.5 °C and −22.1 °C.

The cloudiness is high, with an average of 6/8 and, consequently, insolation is small, with 2 h day^{-1} of average insolation during summer and spring, though the cloud-free days during such seasons show a high irradiance. The relative humidity is very high, with average values above 80 % at JCI and 90 % on the glacier (unpublished data from Agencia Estatal de Meteorología, AEMET).

On the glacier, mass gain is dominated by direct snowfall and wind redistribution of snow, without any contribution from snow avalanches. The glacier ice hardly receives any debris from the surrounding mountains, except at the lowest elevations of its outlets. Tephra layers from the recent eruptions of the neighbouring Deception Island, however, are a common feature of these glaciers (Pallàs et al., 2001).

2 Methods

2.1 AWS data record

The meteorological data used for SEB analysis and as input to the temperature-radiation index melt model was obtained from the AWS located on Johnsons glacier (62°40.266′ N, 60°21.672′ W, 178 m a.s.l. at installation). The AWS (Table 1) was installed on the glacier on 16 December 2006, and the record used herein extends to 15 March 2010. During austral winters, major data gaps exist in the record due to energy shortage. However, for the melt seasons, which we focus on, the data gaps are minor. An ultra-sonic ranger was installed next to the AWS, and was used to measure the relative surface height changes caused by ablation or accumulation. Due to malfunctioning, the ultra-sonic ranger record includes major data gaps throughout the period of measurement.

TCD
5, 3221–3258, 2011

The data sampling and averaging intervals of the AWS logger differ between the summer seasons, when regular visits to the AWS are done from the nearby JCI research station, and the unmanned winter seasons. The majority of the data corresponds to the summer seasons, but still a portion was collected during winter mode of operation. Thus, temporal averages of the meteorological parameters are based on different number of readings. In case of missing data due to gaps or preposterous registrations, hourly averages are calculated down to the representation of at least one reading during the time interval; else linear interpolation between the adjacent time steps was made for gaps up to four hours. A gap in the temperature and relative humidity records due to sensor malfunctioning, spanning the period 16–24 December 2009 was replaced with temperature data from a T107 thermistor installed on the AWS and with RH data from JCI. Offsets calculated from data two days before and after the gap were applied. The temperature sensor was unventilated, which at high short-wave radiation fluxes and low wind speeds exaggerates temperatures and we therefore applied the correction to overheating suggested by Smeets (2006) on all air temperature data.

2.2 Correction of short-wave radiation and albedo

Large pseudo-diurnal variations in albedo (Fig. 2), α, may arise from the poor cosine response of the pyranometeres at high zenith angles and from an instrument set-up non-parallel to the glacier surface. The bias is mainly introduced by the upward facing sensor as incoming solar radiation flux is less diffuse compared to the outgoing (van den Broeke, 2004). As changes of surface conditions affecting α are of gradual nature, with the exception of snow falls, van den Broeke (2004) presented an approach to improve the accuracy of the incoming short-wave fluxes by filtering out diurnal variations using a 24 h running mean "accumulated" albedo, α_d (Eqs. 1 and 2). This approach was subsequently adapted by others (Andreassen et al., 2008; Giesen et al., 2008). α_d is calculated as the ratio between the sums of the instant (measured) outgoing flux, S_r, and the measured incoming solar radiation flux, S_i, with the timing of measurement

TCD
5, 3221–3258, 2011

as midpoint. A corrected incoming short-wave flux, S_d, is there after calculated.

$$\alpha_d = \left(\sum_{t-12\,h}^{t+12\,h} S_r / \sum_{t-12\,h}^{t+12\,h} S_i \right), \quad (1)$$

where t is time in hours (h).

$$S_d = S_r / \alpha_d \quad (2)$$

Equation (1) produces a smooth diurnal signal of α_d that leaves out the extreme values arisen from measurement shortcomings, which normally occur at high zenith angles. As α_d is based on the sums of the short-wave fluxes, the low fluxes occurring at high zenith angles reduces the impact of the measurement deficiencies on α_d and S_d. However, this approach filters out the rapid variations in α associated with changes in cloud cover also during midday hours when short-wave fluxes are high, which may have significant impact on SEB. The rapid variations are an effect of clouds absorbing radiation to a higher degree in the near-infrared spectra, leaving a higher portion of the visible wave lengths to reach the ground, for which the snow reflectance is higher. This effect is further enhanced by multiple reflections between the surface and the cloud base (Warren, 1982; Cutler and Munro, 1996).

With Eqs. (3) and (4) we present and use an extension of Eq. (1) which yields a corrected albedo, α_c, and corrected short-wave flux, S_c, that restore the effect of clouds reasonably well:

$$\alpha_c = \left(\sum_{t-12\,h}^{t+12\,h} S_r / \sum_{t-12\,h}^{t+12\,h} S_i + \lambda(\theta_i - \theta_d) \right) \quad (3)$$

$$S_c = S_r / \alpha_c \quad (4)$$

where λ is the slope of the linear relation between the change in instant albedo, α_i, and the instant fraction of potential top of atmosphere radiation that reaches the ground, θ_i,

TCD
5, 3221–3258, 2011

between two subsequent recording time steps (Fig. 3). The term restoring the effect of clouds is proportional to the difference between θ_i and its corresponding 24 h running mean, θ_d, and scaled by λ. θ_i is calculated as

$$\theta_i = \frac{S_c}{I_{toa}}, \quad (5)$$

where the top of atmosphere radiation, I_{toa}, is given by

$$I_{toa} = I_S(d/d_m)^2 \cos Z, \quad (6)$$

I_S is the solar constant (1366 W m^{-2}), d and d_m are the instant and mean Sun to Earth distance, and Z is the local solar zenith angle. A freely available Matlab code based on Reda and Andreas (2008) was used to calculate the required parameters. An iterative procedure is needed for solving Eq. (3) and subsequently Eq. (4) as Eq. (5) uses S_c as input. The result normally stabilizes after less than five iterations.

Regression analysis to obtain the linear slope λ was applied to each of the four seasonal data sets on all data when zenith angle was 80° or less. The resulting four λ values were all within -0.09 ± 0.01 with corresponding r-values between -0.59 and -0.48. Consequently, λ was statically set to -0.09 in Eq. (3). The daily mean α will be the same regardless of using S_i, S_d or S_c as incoming short-wave flux.

Jonsell et al. (2003) found only a limited effect of clouds on α during ice conditions, probably because the multiple reflection of radiation will be limited due to lower α. The location of the AWS was snow covered during the period of data collection, with the exception of a few days at the end of the melt season 2006/2007, but still with α exceeding 0.55, and therefore we applied Eqs. (3) and (4) to the full data set. The rapid shifts in α_c due to sudden changes in S_c are well represented. During early morning and late afternoon hours an offset towards higher α_c is present. This is due to reduced θ_i caused by the longer atmospheric pathway and increased scattering of solar radiation at high zenith angles, and thus it is not primarily an effect of clouds. However, during the morning and afternoon hours S_c is small and the impact on SEB is

TCD
5, 3221–3258, 2011

limited, while the correction by Eqs. (3) and (4) during midday hours, when S_c is large, will have greater importance for SEB.

2.3 Energy balance calculation

We calculate SEB, using hourly mean AWS data, to investigate the absolute and relative contribution of the energy fluxes involved in glacier heating and melt. The energy balance condition at the glacier surface is represented by the equation

$$S_n + L_{in} + L_{out} + H + E + G + M = 0, \quad (7)$$

Where S_n is the net short-wave flux, L_{in} and L_{out} are the incoming and outgoing long-wave fluxes, respectively, H is the sensible heat flux, and E is the latent heat flux, which summed up are expressed as the atmospheric energy fluxes, A, and must balance the sum of ground heat flux, G, and melt energy flux, M. A flux is considered to be positive when directed towards the surface. We do not quantify the energy from the sensible heat of rain fall due to lack of precipitation measurements on the glacier, but this term is generally small (Hock, 2005). The long-wave radiation components are, in contrast to their short-wave counterparts, treated separately. This division mirrors better their different physical nature and their different response to atmospheric and surface conditions (Ohmura, 2001).

We use the bulk aerodynamic method based on Monin-Obukhov length following Hock and Holmgren (2005). No field measurements of the roughness length for momentum (Z_{0w}) are available for the site. Although Z_{0w} is expected to vary with time (Brock et al., 2000; Hock, 2005), we use Z_{0w} as a constant-in-time model parameter to fit the SEB to the ablation rates estimated from the surface lowering registered by the ultra-sonic ranger. Conversion from surface lowering to mass loss was made by using depth density relations from snow pits dug in the area. The roughness lengths for heat, Z_{0T}, and moisture, Z_{0e}, are treated as functions of Z_{0w} following Andreas (1987). For stable stratification we use the stability functions by Beljaars and Holtslag (1991), and

TCD
5, 3221–3258, 2011

for unstable conditions the expression by Panofsky and Dutton (1984). The best fit was obtained using $Z_{0w} = 1 \times 10^{-4}$ m.

Surface temperature, T_s, in °C, is calculated from L_{out} assuming emissivity of unity:

$$T_s = \begin{cases} (L_{out}/\sigma)^{(1/4)} - 273.15 & , L_{out} \leq 315.6\,\mathrm{W\,m^{-2}}, \\ 0 & , L_{out} > 315.6\,\mathrm{W\,m^{-2}}, \end{cases} \quad (8)$$

where σ is the Stefan-Boltzmann constant (5.67×10^{-8}).

When E is negative, the phase change is considered as sublimation, while when it is positive it is considered as condensation or as resublimation, depending on whether T_s equals or is lower than 0°C.

G could not be captured by any of the sensors of the AWS. On a perfectly temperate glacier G is by definition zero. The Hurd Peninsula glaciers are of polythermal type (Navarro at al., 2009) and during the melt season G will be directed to heat the cold surface layer. From other studies (see table in Ohmura, 2001) we conclude that the average G will be limited to a few $\mathrm{W\,m^{-2}}$, but will occasionally be high due to the release of latent heat at refreezing of melt water upon the first onset of melt in the summer, and during subsequent recommences of melt-refreeze cycles. During the ablation season, melting conditions at the Hurd Peninsula glaciers are repeatedly interrupted by refreezing events. In other modelling approaches, the quantification of the energy compensation needed to reach melting conditions after a period of freezing and cooling of the surface (negative A) differs from full compensation (van de Wal and Russel, 1994) to no compensation (Hock and Holmgren, 2005). The latter means that, as soon as A turns positive, melting is resumed. Hock and Holmgren (2005) argued that the positive compensation flux will just be a part of the accumulated negative flux, because the latent heat from percolating refreezing melt water will make a significant contribution to the reheating of the cooled volume when melt conditions resume at the surface.

We consider the surface to be melting when $T_s > -0.5$ °C and we set G constant to $5\,\mathrm{W\,m^{-2}}$ during melting. The temperature offset from zero degrees is made to allow for melting at depths below the surface skin layer that T_s is representing. Sub-surface

TCD
5, 3221–3258, 2011

melting at sub-zero T_s can occur because of the ability of short-wave radiation to penetrate into the snow cover, where the thermal conductivity is low (Koh and Jordan, 1995). We consider that the surface is refreezing and cooling when A turns negative, and to be heated to resume to melt conditions when A is positive and $T_s < -0.5\,^{\circ}\mathrm{C}$. Thus G balances A during non-melting conditions. In practice this implies that the refreezing flux (negative A) is compensated by the positive flux of A when $T_s < -0.5\,^{\circ}\mathrm{C}$. Melt rates calculated via the energy balance are converted to water equivalent (w.e.) using the latent heat of fusion ($334 \times 10^{-3}\,\mathrm{J\,kg^{-1}}$).

Following Sicart et al. (2008), we describe the relative contribution of the energy fluxes to the variation of A as

$$\rho_x = \frac{r_x \sigma_x}{\sigma_A}, \tag{9}$$

where r_x is the correlation coefficient of flux x to A, and σ_x,σ_A are their respective standard deviations. The sum of ρ_x for all fluxes contributing to A is one.

2.4 Temperature index model description

We performed the surface melt modelling and the sensitivity analysis to perturbations in meteorological conditions using a grid-based distributed temperature-radiation index model following Hock (1999):

$$M_{xy} = \begin{cases} T_{xy}(D_{xy}\delta_{\mathrm{snow/ice}} + m), & T_{xy} \geq 0 \\ 0, & T_{xy} \leq 0 \end{cases} \tag{10}$$

where M_{xy} is the modelled melt at a specific grid cell. The melt factor, m, and the surface specific radiation factor, $\delta_{\mathrm{snow/ice}}$, are model parameters obtained via calibration. The temperature at a specific grid cell, T_{xy}, is given by the AWS temperature record with an offset based on altitude difference and air temperature lapse rate. D is a representation of the direct solar radiation flux and is distributed over the glacier surface depending on the angle of incidence of the solar beam, and scaled from clear-sky

TCD
5, 3221–3258, 2011

conditions using θ_i:

$$D = I_S(\frac{d}{d_m})^2 (\cos\beta \cos Z + \sin\beta \sin Z \cos(\Omega - \Theta)) \theta_i, \quad (11)$$

where Z is the solar zenith angle, Ω is the solar azimuth, β is the surface slope angle and Θ is the surface aspect. We considered Z and Ω to be spatially constant in the study area, while we calculated β and Θ from a digital elevation model (DEM). The DEM has a grid cell resolution of 25 m and was obtained by kriging interpolation from 852 points surveyed in 2000/2001. The surrounding rock topography was digitized from Servicio Geográfico del Ejército 1:25000 map for Hurd Peninsula (SGE, 1991).

A shaded grid cell implies that D is set to zero. We calculated the shading of grid cells by applying standard geometry on the DEM. When the AWS is shaded in the sunset, the preceding non-shaded value of θ_i is used to calculate non-shaded grid cells, while the subsequent non-shaded value is used in the sunrise.

We initialized the model with a distributed snow cover thickness which is continuously reduced with the daily modelled melt and increased in case snow fall was registered by the ultra-sonic ranger. We distributed the snow fall following the mean accumulation pattern obtained from determining the mass balance by the glaciological method for the period 2001–2010 (Navarro et al., 2011). We obtained the initial snow cover grid of each season by interpolating snow depth measurements conducted simultaneously to the first stake height reading, and converting it into mass loss using the density measurements from three snow pits conducted at the beginning of the melt season.

2.5 Temperature-radiation index model calibration

The model calibration is based on comparing the mass balance, b, of a number of stakes obtained by the glaciological method (Navarro et al., 2011) and the model results for the grid cells corresponding to the stake positions. As Eq. (10) is set to compute melt during a specific period and not b, snow fall rates registered by the ultra-sonic ranger (Fig. 4) were distributed over the glacier and subtracted from the modelled

TCD
5, 3221–3258, 2011

melt to produce comparable figures. We assumed a snow density of 300 kg m^{-3} for fresh snow.

We converted the stake height differences into water equivalents using the density measurements from three snow pits at the beginning and the end of the melt season. As densification of the snow pack due to refreezing of melt water is expected during the melt season, the total mass loss at each stake in the end of the calibration period is given by the beginning of the season mass minus the end of the season mass. On average, the end of melt season densities were 14 % higher. Snow density is however expected to show local variations and introduces a source of error. Based on extensive density measurements during 2004–2010 on Johnsons and Hurd glaciers (Navarro et al., 2011), the relative double standard deviation of all measured snow densities was 13 % and provides an indication on the error involved. Where the model indicates ice at the surface, we used a density of 900 kg m^{-3} to convert into water equivalents.

Among the four seasons with data available from the AWS, we chose the period 29/11/2008–10/02/2009 as calibration period as it provided the best combination of the following criteria: number of stakes, length of calibration period, high ablation rates, and number of stakes on ice surface at the end of the period. For the calibration period 2008/2009 the total snowfall registered by the ultra-sonic ranger was 0.05 m w.e.

We calibrated the model parameters to obtain the least mean root square error between modelled and measured b (Fig. 5, Table 2), with the criteria that $\sigma_{\text{ice}} > \sigma_{\text{snow}}$ to reflect the higher absorption of short-wave radiation on an ice surface. As pointed out by others (Hock, 1999; Schuler et al., 2007), the calibration of the current formulation of the model is not unambiguous as it is possible to find different sets of tuning parameters giving equally good fits to the observed data. Based on best performance in the subsequent validation of the model, we used $m = 0.092$ mm h^{-1} K^{-1}, $\delta_{\text{snow}} = 1.9 \times 10^{-3}$ mm m^2 W^{-1} h^{-1} K^{-1}, and $\delta_{\text{ice}} = 4.4 \times 10^{-3}$ mm m^2 W^{-1} h^{-1} K^{-1}.

TCD
5, 3221–3258, 2011

3 Results and discussion

3.1 Temperature and energy fluxes during the melt seasons

For simple comparison, we set the periods of SEB analysis to a standard melt season 15 December–15 March, which corresponds to the period with most surface melt. Melt seasons are characterized by a mean temperature close to zero (Table 3). Hourly mean temperature rarely deviates more than $\pm 5\,^{\circ}\mathrm{C}$ from zero (Fig. 6), due to the maritime setting of the glaciers. Maximum (minimum) hourly mean temperature during the four seasons was $6.8\,^{\circ}\mathrm{C}$ ($-8.2\,^{\circ}\mathrm{C}$) and the four seasonal mean temperatures ranged within $0.7\,^{\circ}\mathrm{C}$. Seasonal mean α showed only small variations and was lowest in 2006/2007, which was the only season when ice surfaced at the location of the AWS.

For all seasons the main energy source (sink) was L_{in} (L_{out}) and the resulting mean long-wave net flux was negative. The net short-wave flux, S_{n}, together with L_{in}, show the highest inter-seasonal variations, but are opposing each other yielding a reduced variation in mean seasonal A to a maximum of $5\,\mathrm{W\,m^{-2}}$, which is equivalent to 0.11 m w.e. of melt for a full melt season. The inter-seasonal variation in S_{n} is driven, with similar weights, by the variations in α and S_{c}. S_{n} was for all seasons the individual source with best fit to A (Table 4) and was also, expressed as ρ, the flux having the highest influence on the variation of A. In 2009/2010 ρ was 120 %, as the variation was counteracted by L_{in}. The generally negative coupling between L_{in} and S_{n} is mainly an effect of their different response to cloud cover. ρ for L_{in} varies between the individual seasons from positive, through insignificant, to negative. This reflects the complex balancing of A as a response to the meteorological conditions and is exemplified in Fig. 7. During 2009/2010 the anti-correlation between S_{n} and L_{in} was strong and days with high daily mean A were in general associated with the outer ranges of S_{n} compared to the season 2006/2007, when anti-correlation was weak and days with high A were in general associated with intermediate daily mean S_{n}. The standard deviation of S_{c} was higher in 2009/2010, indicating a season with more contrast between clear and cloudy days, which may explain the different modes.

TCD
5, 3221–3258, 2011

The negative coupling between L_{in} and S_n results in a high correspondence between net radiation, R, and A. R explains up to 82 % of the variation of A for an individual season. The turbulent fluxes, H and E, have, considering their low mean absolute values, a proportionally large impact on the variation of A that was largest in 2008/2009, when they together explain a third of the variance of A while the influence of S_n was reduced. The coupling between T_{air} and the energy fluxes constituting A is the physical basis of the temperature-index models. T_{air} was best correlated with A during the seasons 2006/2007 and 2008/2009, coinciding with the highest ρ of L_{in}. T_{air} and S_n were slightly negatively or insignificantly correlated, with the highest correlation factor (−0.47) occurring in 2007/2008. The generally low correspondence between A and T_{air}, in particular for 2007/2008 and 2009/2010, is discouraging for using a solely temperature-driven ablation model, both at point scale and distributed over the glacier. The degree of explanation for the variation of A when using a combination of T_{air} and S_n becomes similar for all seasons and is just slightly lower than the corresponding degree of explanation for R. In a combination where S_n is substituted by D, thus corresponding to the input parameters in the temperature radiation-index model (Fig. 8), the degree of explanation is only slightly lower. Using a distributed model driven by D instead of S_n reduces the complexity and avoids the source of error associated with introducing a spatial and temporal modelling of α that is required for a model driven by S_n.

3.2 Model validation and sensitivity analysis

The calibrated model was run on three periods from other melt seasons for which corresponding stake measurements and data from AWS were available (Table 2). The period from season 2006/2007 is significantly shorter than the others because the installation of the AWS took place several weeks after the first stake reading of the season and thus the period of correspondence starts with the second set of stake readings of the season.

The modelled b generally agrees well with b obtained by the glaciological method (Table 2). The difference is largest for season 2007/2008, when the model

TCD
5, 3221–3258, 2011

underestimates b by 0.14 m w.e., which is slightly larger than the typical error of the glaciological method (ca. 0.1 m w.e.; Jansson, 1999). The scatter from a linear relation between observed and modelled b is large for the short validation period 2006/2007. This might be explained by the fact that during the validation period a large part of the surface at the position of the stakes changed from snow to ice conditions, and thus the actual more gradual transition between snow and ice compared to the model's binary set-up, may reduce the model performance. b in 2009/2010 was small because of a combination of little melt and extensive snow fall. The discrepancies between the modelled and the observed distributions of the snow fall possibly introduces a significantly larger error compared to the other years, which is exemplified by an outlier that was falsely modelled as ice surface for much of the period. The difference in seasonal mean T_{air} and D is modest. A higher inter-seasonal variation, reflecting more contrasting weather conditions between the periods, would possibly have enhanced the validity test of the model.

We analyzed the sensitivity of the model by applying perturbations to the calibrated model parameters, and to the meteorological parameters by manipulating the original AWS data corresponding to the calibration period.

Changes in m by ± 10 % produce a change in melt of a few percent (Fig. 9), while a similar change in $\delta_{snow/ice}$ varies the total modelled melt by about ± 10 % (or ± 0.05 m w.e.). A change by ± 50 % in snow cover thickness over the entire glacier surface, that influences the temporal and spatial distribution of snow and ice represented in the model through variations in the use of δ_{snow} or δ_{ice}, changes the melt rates by less than 10 %.

We run the model with a step increase of 0.5 °C in T_{air}, which is of the same magnitude as one standard deviation of the summer mean temperature for the last 30 years from the nearest long-term temperature instrument record (Bellinghausen Station on King George Island) and close to half a standard variation of the daily mean T_{air} for the calibration period. The corresponding modelled melt rates increased by 56 % to 0.81 m w.e. A temperature decrease of the same magnitude resulted in a reduction

TCD
5, 3221–3258, 2011

of melt by 44 % to 0.30 m w.e. There is a strong temperature threshold effect which is illustrated by the change in number of grid cells integrated over all the time steps where the model indicates melting conditions. For the temperature increase (decrease) scenario the change was +52 % (−54 %).

Mean T_{air} for the validation period 2009/2010 was 0.5 °C colder than that of the calibration season 2008/2009, while D and S_n registered at the AWS were similar. The periods are of similar lengths and we note that the measured melt rate in 2009/2010 was 38 % lower than the melt measured in 2008/2009, which is close to the modelled response to a 0.5 °C temperature decrease on the 2008/2009 data.

Because of the limited elevation range of the glacier, the entire glacier area experiences temperatures flickering around zero during summer time. This leads to a high sensitivity to temperature changes during the melt seasons.

We perturbed the radiation climate represented in the model by changing θ_i, as the other inputs to obtain D are not related to the meteorological conditions on the glacier. We run the model with a step change in θ_i that, just as in the T_{air} scenario, corresponds to half a standard deviation of the daily means (0.06). An increase in θ_i (implying more direct solar radiation) leads to 15 % more melt (0.08 m w.e.), and a similar decrease in melt for a corresponding decrease in θ_i.

T_{air} and θ_i are anti-correlated in the AWS record, meaning that under present climate a temperature increase is in general associated with a cloudier sky. Extrapolating this to a temperature increase driven by climate change implies that an increased melt due to higher temperature will to some extent be balanced by reduced direct radiation. However, climate change at these latitudes will probably be mainly driven by the associated changes in cyclonic activity and pathways, hence changes will neither be static nor solely impact a single meteorological parameter, and the model sensitivity as a predictive tool provides only a first level of understanding.

TCD
5, 3221–3258, 2011

4 Conclusions

We have used an AWS record located on Hurd Peninsula glaciers, Livingston Island, to analyse the SEB for four melt seasons (2006/2007–2009/2010). Further, we set up and run a temperature-radiation index model. The model was calibrated and validated with b obtained with the glaciological method. A novel correction method of α_i, which adds the diurnal variation of clouds on a 24 h running mean α, is presented and adopted. The advantage of the method is that the rapid and large variations during the high fluxes at midday in the short-wave balance are better reproduced. The following main conclusions can be drawn from our analysis:

1. S_n is the most important individual energy flux impacting on the variation in A, but using the combined expression of the radiation fluxes, R, the degree of explanation increases and can account for 76–82 % of the variation in A. This high degree of explanation is due to a balancing of the generally anti-correlated fluxes S_n and L_{in}, which is mainly an effect of their different response to cloud cover.

2. The seasonal means of T_{air} at the AWS site are close to zero during the four melt seasons, and due to the small altitude range of the glaciers their whole area shows temperatures flickering around zero degrees during the summer season. The poor correlation factors between daily mean T_{air} and A questions the performance of a solely temperature-based melt model, both at point scale and distributed over the glacier, and supports the use of a temperature radiation-index model. A combination of T_{air} with S_n or D increases the correlation factor at the point scale.

3. The modelled mass balance is in good agreement with that obtained by the glaciological method, showing differences model-observations generally below the typical error of the glaciological method (ca. 0.1 m w.e., Jansson, 1999), with no significant bias.

TCD
5, 3221–3258, 2011

4. The model results show that these glaciers are very sensitive to air temperature changes. An increase (decrease) in temperature of 0.5 °C implies an increase (decrease) of the melt rates by about 56 % (44 %), which is an effect of the strong zero degree threshold for onset of melt. The high model sensitivity of these glaciers to temperature change are indicative, but it must be noted that it only provides a first level of understanding of the response of the glacier mass balance to real climatic changes.

5. An increase (decrease) in the fraction of potential top of atmosphere radiation that reaches the ground, θ_i, by half a standard deviation of its daily mean leads to an increase (decrease) of melt by 15 %.

TCD
5, 3221–3258, 2011

List of symbols

A	– atmospheric energy fluxes = $R + H + E$
b	– mass balance
d and d_m	– instant and mean Sun to Earth distance
D	– representation of the direct solar radiation flux (according to Eq. 11)
E	– latent heat flux
G	– ground heat flux
H	– sensible heat flux
I_S	– solar constant (1366 W m^{-2})
I_{toa}	– top of atmosphere radiation
L_{in} and L_{out}	– incoming and outgoing long-wave fluxes
m	– melt factor
M	– melt energy flux
r_x	– correlation coefficient of flux x to A
R	– net radiation
S_c	– corrected (according to Eq. 4) incoming short-wave flux
S_d	– corrected (according to Eq. 2) incoming short-wave flux
S_i	– measured incoming solar radiation flux
S_n	– net short-wave flux = $S_c + S_r$
S_r	– instant measured outgoing short-wave flux
T_{air}	– air temperature
T_s	– surface temperature
X_{xy}	– value of variable X at a specific grid cell
Z	– solar zenith angle
Z_{0e}	– roughness length for moisture
Z_{0T}	– roughness length for heat
Z_{0w}	– roughness length for momentum
α	– albedo
α_c	– corrected (according to Eq. 3) albedo
α_d	– corrected (according to Eq. 1) albedo
α_i	– instant albedo
β	– surface slope angle
$\delta_{snow/ice}$	– radiation factor of snow/ice
λ	– slope of linear relation between the change in α_i and θ_i, between two subsequent time steps
Ω	– solar azimuth
ρ_x	– relative contribution of the energy flux x to the variation of A
σ	– Stefan-Boltzmann constant (5.67 × 10^{-8})
σ_x	– standard deviation of x
θ_i	– instant fraction of potential top of atmosphere radiation that reaches the ground
θ_d	– 24 h running mean of θ_i
Θ	– surface aspect

TCD
5, 3221–3258, 2011

Acknowledgements. We thank all those who participated in the fieldwork, including glaciologists and meteorological and mountain technicians, as well as the teams of JCI station during the different campaigns spanned by our study period. A special mention is owed to AEMET technicians José Vicente Albero and José Juan García-Ayala. Marco Möller is thanked for fruitful comments on the manuscript. This research was funded by projects CGL2005-05483 and CTM2008-05878/ANT from the Ministry of Science and Innovation.

References

Andreas, E. L.: A Theory for the Scalar Roughness and the Scalar Transfer-Coefficients over Snow and Sea Ice, Bound-Lay. Meteorol., 38, 159–184, 1987.

Andreassen, L. M., van den Broeke, M. R., Giesen, R. H., and Oerlemans, J.: A 5 year record of surface energy and mass balance from the ablation zone of Storbreen, Norway, J. Glaciol., 54, 245–258, 2008.

Beljaars, A. C. M. and Holtslag, A. A. M.: Flux Parameterization over Land Surfaces for Atmospheric Models, J. Appl. Meteorol., 30, 327–341, 1991.

Braun, M. and Hock, R.: Spatially distributed surface energy balance and ablation modeling of the ice cap of King George Island (Antarctica), Global Planet. Change, 42, 45–48, 2004.

Brock, B. W., Willis, I. C., Sharp, M. J., and Arnold, N. S.: Modelling seasonal and spatial variations in the surface energy balance of Haut Glacier d'Arolla, Switzerland, Ann. Glaciol., 31, 53–62, 2000.

Cook, A. J., Fox, A. J., Vaughan, D. G., and Ferrigno, J. G.: Retreating glacier fronts on the Antarctic Peninsula over the past half-century, Science, 308, 541–544, 2005.

Cutler, P. M. and Munro, D. S.: Visible and near-infrared reflectivity during the ablation period on Peyto Glacier, Alberta, Canada, J. Glaciol., 42, 333–340, 1996.

Giesen, R. H., van den Broeke, M. R., Oerlemans, J., and Andreassen, L. M.: Surface energy balance in the ablation zone of Midtdalsbreen, a glacier in southern Norway: Interannual variability and the effect of clouds, J. Geophys. Res., 113, D21111, doi:1029/2008JD010390, 2008.

Greuell, W. and Genthon, C.: Modelling land an ice surface mass balance, in: Mass balance of the cryosphere: Observations and modelling of contemporary and future climate change,

TCD

5, 3221–3258, 2011

edited by: Bamber, J. L. and Payne, A. J., 117–168, Cambridge University Press, Cambridge, UK, 2004.
Hock, R.: A distributed temperature-index ice- and snowmelt model including potential direct solar radiation, J. Glaciol., 45, 101–111, 1999.
Hock, R.: Glacier melt: a review of processes and their modelling, Prog. Phys. Geog., 29, 362–391, 2005.
Hock, R. and Holmgren, B.: A distributed surface energy-balance model for complex topography and its application to Storglaciaren, Sweden, J. Glaciol., 51, 25–36, 2005.
Hulth, J., Rolstad, C., Trondsen, K., and Rodby, R. W.: Surface mass and energy balance of Sorbreen, Jan Mayen, 2008, Ann. Glaciol., 51, 110–119, 2010.
Jansson, P.: Effect of uncertainties in measured variables on the calculated mass balance of Storglaciären, Geogr. Ann., 81A, 633–642, 1999.
Jonsell, U., Hock, R., and Holmgren, B.: Spatial and temporal variations in albedo on Storglaciaren, Sweden, J. Glaciol., 49, 59–68, 2003.
Koh, G. and Jordan, R.: Subsurface melting in a seasonal snow cover, J. Glaciol., 41, 474–482, 1995.
Molina, C., Navarro, F. J., Calvet, J., García-Sellés, D., and Lapazaran, J. J.: Hurd Peninsula glaciers, Livingston Island, Antarctica, as indicators of regional warming: ice volume changes during the period 1956–2000, Ann. Glaciol., 46, 43–49, 2007.
Möller, M., Finkelnburg, R., Braun, M., Hock, R., Jonsell, U., Pohjola, V., Scherer, D., and Schneider, C.: Climatic mass balance of the ice cap Vestfonna, Svalbard – a spatially distributed assessment using ERA-Interim and MODIS data, J. Geophys. Res., 116, F03009, doi:10.1029/2010JF001905, 2011.
Navarro, F. J., Otero, J., Macheret, Yu. Ya., Vasilenko, E. V., Lapazaran, J. J., Ahlstrøm, A. P., and Machío, F.: Radioglaciological studies on Hurd Peninsula glaciers, Livingston Island, Antarctica, Ann. Glaciol., 50, 17–24, 2009.
Navarro, F. J., Jonsell, U. Y., Corcuera, M. I., and Martín-Español, A.: Decelerated mass loss of Hurd and Johnsons glaciers, Livingston Island, Antarctic Peninsula, in spite of continued regional warming, in prep., 2011.
Ohmura, A.: Physical basis for the temperature-based melt-index method, J. Appl. Meteorol., 40, 753–761, 2001.
Otero, J.: Generación automática de malla de elementos finitos en modelos evolutivos de dinámica de glaciares, PhD thesis, Universidad Politécnica de Madrid, Spain, 131 pp., 2008.

TCD
5, 3221–3258, 2011

Otero, J., Navarro, F. J., Martín, C., Cuadrado, M. L., and Corcuera, M. I.: A three-dimensional calving model: numerical experiments on Johnsons Glacier, Livingston Island, Antarctica, J. Glaciol., 56, 200–214, 2010.

Pallàs, R., Smellie, J. L., Casas, J. M., and Calvet, J.: Using tephrochronology to date temperate ice: correlation between ice tephras on Livingston Island and eruptive units on Deception Island volcano (South Shetland Islands, Antarctica), Holocene, 11, 149–160, 2001.

Panofsky, H. A. and Dutton, J. A.: Atmospheric turbulence: models and methods for engineering applications, Wiley-Interscience, New York, USA, 397 pp., 1984.

Pellicciotti, F., Brock, B., Strasser, U., Burlando, P., Funk, M., and Corripio, J.: An enhanced temperature-index glacier melt model including the shortwave radiation balance: development and testing for Haut Glacier d'Arolla, Switzerland, J. Glaciol., 51, 573–587, 2005.

Pritchard, H. D. and Vaughan, D. G.: Widespread acceleration of tidewater glaciers on the Antarctic Peninsula, J. Geophys. Res., 112, F03S29, doi:10.1029/2006JF000597, 2007.

Rau, F., Mauz, F., De Angelis, H., Jaña, R., Arigony Neto, J., Skvarca, P., Vogt, S., Saurer, H., and Gossmann, H.: Variations of glacier frontal positions on Northern Antarctic Peninsula, Ann. Glaciol., 39, 525–530, 2004.

Reda, I. and Andreas, A.: Solar position algorithm for solar radiation application, National Renewable Energy Laboratory (NREL), Golden, Colorado, USA, Technical Rep. NREL/TP-560-34302, 56 pp., 2008.

Rignot, E., Casassa, G., Gogineni, P., Krabill, W., Rivera, A., and Thomas, R.: Accelerated ice discharge from the Antarctic Peninsula following the collapse of Larsen B ice shelf, Geophys. Res. Lett., 31, L18401, doi:10.1029/2004GL020697, 2004.

Rott, H., Skvarca, P., and Nagler, T.: Rapid Collapse of Northern Larsen Ice Shelf, Antarctica, Science, 271, 788–792, doi:10.1126/science.271.5250.788, 1996.

Scambos, T. A., Bohlander, J. A., Shuman, C. A., and Skvarca, P.: Glacier acceleration and thinning after ice shelf collapse in the Larsen B embayment, Antarctica, Geophys. Res. Lett., 31, L18402, doi:10.1029/2004GL020670, 2004.

Schuler, T. V., Hock, R., Jackson, M., Elvehoy, H., Braun, M., Brown, I., and Hagen, J. O.: Distributed mass-balance and climate sensitivity modelling of Engabreen, Norway, Ann. Glaciol., 42, 395–401, 2005.

Schuler, T. V., Loe, E., Taurisano, A., Eiken, T., Hagen, J. O., and Kohler, J.: Calibrating a surface mass balance model for the Austfonna ice cap, Svalbard, Ann. Glaciol., 46, 241–248, 2007.

TCD
5, 3221–3258, 2011

Servicio Geográfico del Ejército (SGE): Livingston Island, Hurd Peninsula, 1:25000 map, 1 Edn., Madrid, Spain, 1991.
Sicart, J. E., Hock, R., and Six, D.: Glacier melt, air temperature, and energy balance in different climates: The Bolivian Tropics, the French Alps, and northern Sweden, J. Geophys. Res., 113, D24113, doi:10.1029/2008JD010406, 2008.
Smeets, C. J. P. P.: Assessing unaspirated temperature measurements using a thermocouple and a physically based model, in: The mass budget of Arctic glaciers. Extended abstracts, Workshop and GLACIODYN Planning Meeting, 29 January-3 February 2006, Obergurgl, Austria, published by the Institute for Marine and Atmospheric Research, Utrecht, The Netherlands, 99-101, 2006.
Turner, J., Colwell, S. R., Marshall, G. J., Lachlan-Cope, T. A., Carleton, A. M., Jones, P. D., Lagun, V., Reid, P. A., and Iagovkina, S.: Antarctic climate change during the last 50 years, Int. J. Climatol., 25, 279–294, 2005.
Turner, J., Bindschadler, R. A., Convey, P., Di Prisco, G., Fahrbach, E., Gutt, J., Hodgson, D. A., Mayewski, P. A., and Summerhayes, C. P.: Antarctic Climate Change and the Environment, Scientific Committee on Antarctic Research, Cambridge, UK, 555 pp., 2009.
van de Wal, R. S. W. and Russel, A. J.: A comparison of energy balance calculations measured ablation and runoff near Sondre Stromfjord, West Greenland, Global Planet. Change, 9, 29–38, 1994.
van den Broeke, M., van As, D., Reijmer, C., and van de Wal, R.: Assessing and improving the quality of unattended radiation observations in Antarctica, J. Atmos. Ocean. Tech, 21, 1417–1431, 2004.
van den Broeke, M.: Strong surface melting preceded collapse of Antarctic Peninsula ice shelf, Geophys. Res. Lett., 32, L12815, doi:10.1029/2005GL023247, 2005.
Vaughan, D. G.: Recent trends in melting conditions on the Antarctic Peninsula and their implications for ice-sheet mass balance and sea level, Arct. Antarct. Alp. Res., 38, 147–152., 2006.
Vaughan, D. G., Marshall, G. J., Connolley, W. M., Parkinson, C., Mulvaney, R., Hodgson, D. A., King, J. C., Pudsey, C. J., and Turner, J.: Recent rapid regional climate warming on the Antarctic Peninsula, Climatic Change, 60, 243–274, 2003.
Warren, S. G.: Optical-Properties of Snow, Rev. Geophys., 20, 67–89, 1982.

TCD
5, 3221–3258, 2011

Table 1. Instruments of the AWS.

Parameter	Sensor	Accuracy
Relative humidity	Vaisala HMP45C	RH ± 2 %@0 °C
Air temperature	Vaisala HMP45C	T_{air} ± 0.3 °C@0 °C
Radiation, four components	Kipp&Zonen CNR1	±10% daily total
Wind speed and direction	Young 05103-45	±0.3 m s^{-1}, ±3°
Surface height	Campbell SR50	±0.01 m

TCD
5, 3221–3258, 2011

Table 2. Characteristics of model calibration and validation runs.

Season	Type	Period	No. of days	No. of stakes	Modelled melt (mm w.e.)	Modelled melt rate (mm day^{-1})	Snow fall (mm w.e.)	Modelled b (mm w.e.)	rms	D (Wm^{-2})	T_{air} (°C)	S (Wm^{-2})	Measured b (mm w.e.)	Measured melt rate (mm day^{-1})
2006/2007	Validation	25 Jan–24 Feb	31	41	280	9.0	15	276	142	142	0.5 ± 1.1	48.7	290	9.8
2007/2008	Validation	05 Dec–20 Feb	78	37	322	4.1	57	280	196	196	−0.2 ± 1.4	47.2	420	6.1
2008/2009	Calibration	29 Nov–10 Feb	74	42	529	7.1	51	481	115	197	0.1 ± 1.2	49.5	430	6.5
2009/2010	Validation	09 Dec–01 Mar	82	36	301	3.7	159	196	161	198	−0.4 ± 1.4	48.0	170	4.0

TCD
5, 3221–3258, 2011

Table 3. Mean daily air temperature (°C), energy fluxes (W m^{-2}), α_c and θ_i with their standard deviations, for the four melt seasons.

Season	T_{air}		S_c		S_n		H		E		L_{in}		L_{out}		R		A		α_c		θ_i	
2006/2007	−0.4	1.9	178	80	56	29	7	8	−3	5	292	25	−311	8	37	22	41	25	0.69	0.07	0.43	0.16
2007/2008	0.3	1.1	166	85	45	29	8	8	1	7	303	20	−315	4	32	19	41	20	0.74	0.05	0.40	0.16
2008/2009	0.4	1.0	165	67	44	22	8	7	−2	7	299	17	−315	4	27	17	34	22	0.72	0.05	0.41	0.13
2009/2010	−0.3	1.2	189	89	52	33	9	8	−5	8	293	25	−313	5	32	17	36	18	0.73	0.05	0.44	0.16

TCD
5, 3221–3258, 2011

Table 4. Correlation coefficient (r), and corresponding ρ to A, for daily mean energy fluxes, T_{air} and combinations of T_{air}, S_n, and D.

Season	H		E		S_n		L_{in}		L_{out}		R		T_{air}	$T_{air}+S_n$	$T_{air}+D$
2006/2007	0.30	9 %	0.46	9 %	0.60	69 %	0.33	33 %	−0.64	−20 %	0.93	82 %	0.70	0.78	0.69
2007/2008	0.22	9 %	0.42	14 %	0.55	83 %	0.01	1 %	−0.37	−7 %	0.78	76 %	0.47	0.76	0.72
2008/2009	0.56	18 %	0.57	19 %	0.43	43 %	0.42	33 %	−0.67	−12 %	0.82	63 %	0.60	0.82	0.73
2009/2010	0.27	11 %	0.16	7 %	0.67	120 %	−0.24	−32 %	−0.22	−6 %	0.87	82 %	0.53	0.78	0.71

TCD
5, 3221–3258, 2011

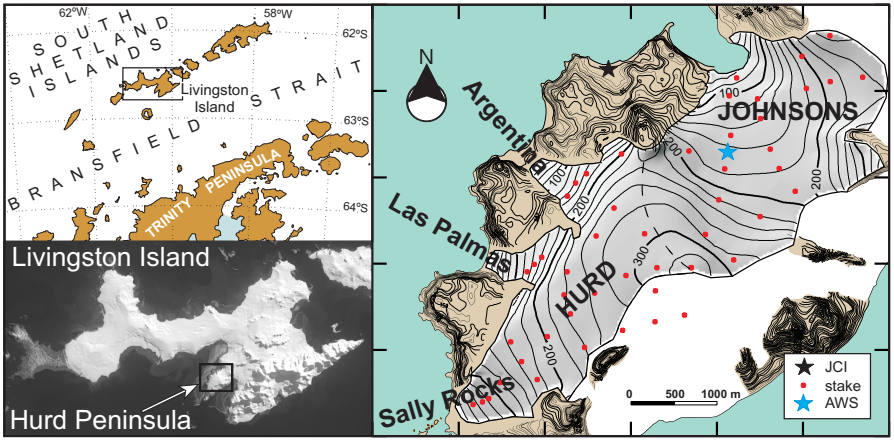

Fig. 1. Location of Hurd Peninsula, Livingston Island, with the position of Juan Carlos I Station (JCI), the AWS and the mass balance stakes in 2008/2009.

TCD
5, 3221–3258, 2011

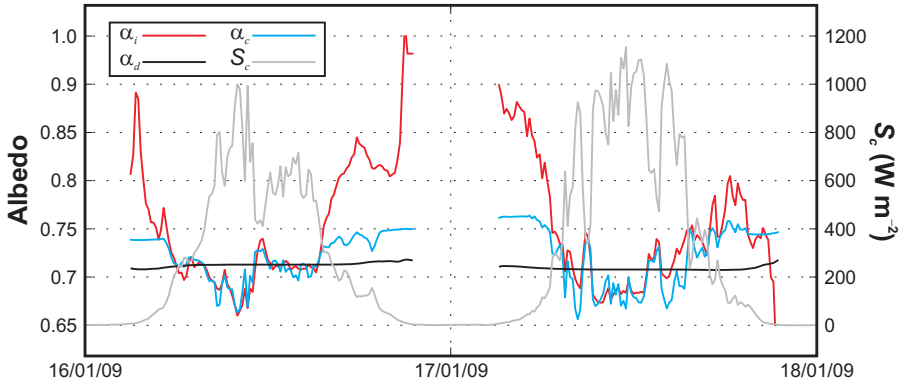

Fig. 2. Example of diurnal variation in α_i, α_d, α_c and S_c.

TCD
5, 3221–3258, 2011

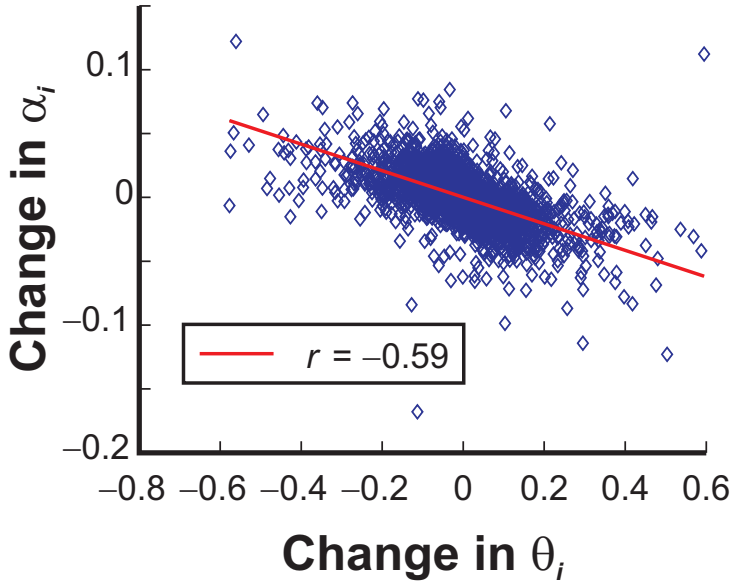

Fig. 3. Change in θ_i versus change in α_i between subsequent AWS recording time steps (10 min) for the melt season 2007/2008. The linear fit has slope −0.10.

TCD
5, 3221–3258, 2011

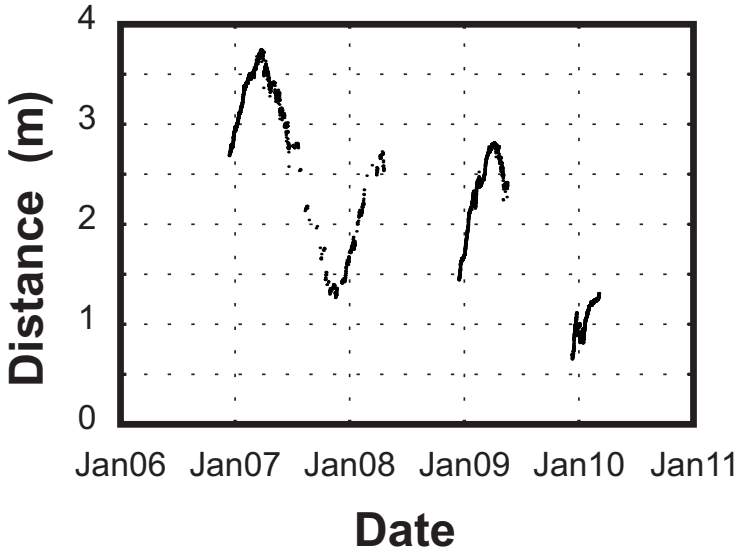

Fig. 4. Distance to snow surface registered by the ultra-sonic ranger.

TCD
5, 3221–3258, 2011

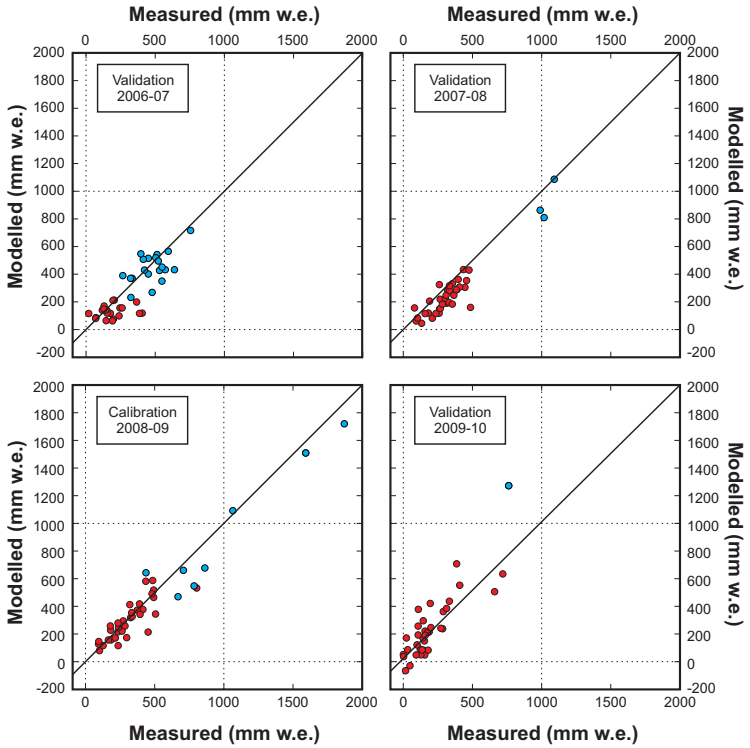

Fig. 5. Measured and modelled point *b* of the individual ablation stakes for the calibration and validation runs (mm w.e.). Blue dots indicate that the model handled the surface of the position of the stake as ice at the end of the modelled period.

TCD
5, 3221–3258, 2011

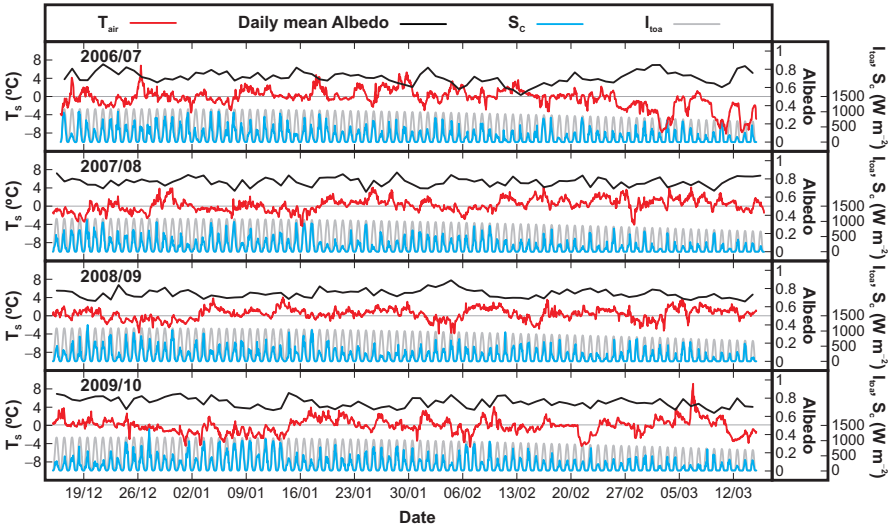

Fig. 6. Hourly T_{air}, S_c, I_{toa} and daily mean α for the four melt seasons 2006/2007–2009/2010 defined as 15 December–15 March.

TCD
5, 3221–3258, 2011

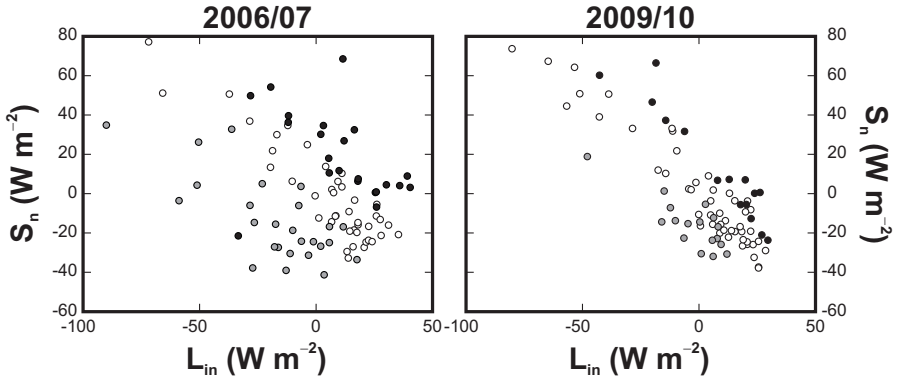

Fig. 7. Daily mean offset to the seasonal mean L_{in} versus corresponding S_n for melt seasons 2006/2007 and 2009/2010. Black dots indicate days when A was larger than 150 % of seasonal mean A, grey dots when lower than 50 % and white dots when A was between 50 % and 150 %.

TCD
5, 3221–3258, 2011

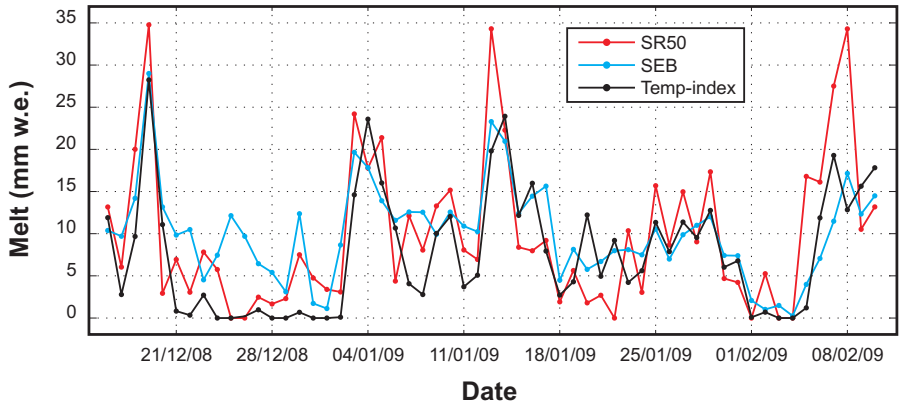

Fig. 8. Surface melt at the position of the AWS according to the surface lowering registered by the ultra-sonic ranger (SR50), SEB calculations and temperature-radiation index model. The time period corresponds to the calibration period of the temperature index model.

TCD
5, 3221–3258, 2011

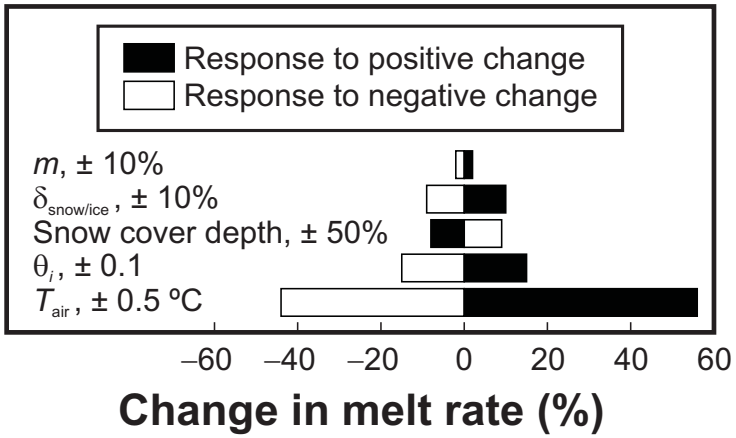

Fig. 9. Change in melt rate for the Hurd Peninsula glaciers resulting from perturbation in various parameters relative to the calibrated run of the 2008/2009 AWS data.

TCD
5, 3221–3258, 2011